Nanoscale

COMMUNICATION

View Article Online
View Journal | View Issue

Cite this: *Nanoscale*, 2015, **7**, 2862

Received 31st October 2014,
Accepted 6th January 2015

DOI: 10.1039/c4nr06429a

www.rsc.org/nanoscale

Plasmonic core–shell nanoparticles for SERS detection of the pesticide thiram: size- and shape-dependent Raman enhancement†

Pengzhen Guo,[a,b,c] Debabrata Sikdar,[d] Xiqiang Huang,*[a] Kae Jye Si,[b,c] Wei Xiong,[b,c] Shu Gong,[b,c] Lim Wei Yap,[b,c] Malin Premaratne[d] and Wenlong Cheng*[b,c]

We systematically investigated the size- and shape-dependent SERS activities of plasmonic core–shell nanoparticles towards detection of the pesticide thiram. Monodisperse Au@Ag nanocubes (NCs) and Au@Ag nanocuboids (NBs) were synthesized and their Ag shell thickness was precisely adjusted from ~1 nm to ~16 nm. All these nanoparticles were used as SERS substrates for thiram detection, and the Raman intensities with three different lasers (514 nm, 633 nm and 782 nm) were recorded and compared. Our results clearly show that: (1) the excitation wavelength discriminated particle shapes regardless of particle sizes, and the maximized Raman enhancement was observed when the excitation wavelength approaches the SERS peak (provided there is significant local electric field confinement on the plasmonic nanostructures at that wavelength); (2) at the optimized laser wavelength, the maximum Raman enhancement was achieved at a certain threshold of particle size (or silver coating thickness). By exciting particles at their optimized sizes with the corresponding optimized laser wavelengths, we achieved a detection limit of roughly around 100 pM and 80 pM for NCs and NBs, respectively.

Introduction

Surface enhanced Raman spectroscopy (SERS) is a unique spectroscopic tool for identification of unique signature (fingerprint) information of chemical and biological species.[1–9] SERS can be used to detect a wide range of analytes, such as explosives,[10,11] narcotics,[12,13] and pesticides.[14] Despite encouraging theoretical and experimental advances of SERS over the past few decades, its potential has yet to be realized due to the challenges in fabricating SERS-active substrates with high sensitivity and reproducibility. Three representative SERS substrates are structured noble metal surfaces typically manufactured by electrochemical or lithographical techniques; colloidal metal nanoparticle aggregates/assemblies; individual metal nanoparticles.

The latter two types of SERS substrates require synthesis of colloidal metal nanoparticles. It has been demonstrated that key structural parameters such as particle sizes and shapes and compositions play a critical role in determining SERS signatures.[15–17] This is because the nanoparticle plasmons responsible for the SERS enhancements are strongly dependent on these structural parameters. The past two decades have seen substantial progress in wet chemistry synthesis of structurally well-defined noble metal nanoparticles with respect to precise size and shape control. This enables the formulation of the 'so-called' artificial periodic table,[18] offering virtually unlimited possibilities for tailoring plasmonic properties for SERS enhancement.

Compared to single-element particles, bimetallic nanoparticles provide richer plasmonic modes owing to their combined material-dependent and size/shape-dependent plasmonics.[19–23] In particular, Au@Ag core–shell spherical nanoparticles have recently been used as SERS substrates for detecting thiram[24] and 1-naphthalenethiol.[25] The enhancement was found to be contributed by individual particles rather than aggregates—an advantage for intimate surface adsorption of targets[13,17,24,26] in contrast to ineffective target diffusion into the particle aggregates.[27] This result paved the way for utilizing core–shell particle for surface identification and quantitative detection of pesticide residues at various peels of fruits.[24] In addition, Au@Ag core–shell nanoparticles were also found to exhibit higher SERS enhancement than monometallic Au or Ag nanoparticles of similar size under near-infrared excitation.[25]

[a]*Department of Physics, Harbin Institute of Technology, Harbin, Heilongjiang Province 150080, P.R. China. E-mail: huangxq@hit.edu.cn*
[b]*Department of Chemical Engineering, Monash University, Clayton, Victoria 3800, Australia. E-mail: wenlong.cheng@monash.edu*
[c]*The Melbourne Centre for Nanofabrication, Clayton, Victoria 3800, Australia*
[d]*Advanced Computing and Simulation Laboratory (AχL), Department of Electrical and Computer Systems Engineering, Monash University, Clayton 3800, Victoria, Australia*

†Electronic supplementary information (ESI) available: Raman spectra of 10^{-6} M thiram based on NCs and NBs with increasing sizes; Raman spectra of 10^{-10} M thiram based on NC30 and 0.8×10^{-10} M thiram based on NB15; the optical spectra of ~2.2 and ~4.1 aspect ratio gold nanorods and nanocuboids; SERS activities and detecting limit of thiram varying with aspect ratio of gold nanorod core. See DOI: 10.1039/c4nr06429a

Here, we extend previous studies in spherical core–shell nanoparticles to non-spherical core–shell nanoparticles with a focus on understanding size- and shape-dependent SERS enhancement. We exploited Au@Ag core–shell nanocubes and nanocuboids as SERS-active particles and systematically compared their SERS activities towards detection of pesticide thiram which is a dithiocarbamate fungicide. Our results clearly show that the excitation wavelength discriminated particle shapes regardless of particle sizes, and maximized Raman enhancement was observed at a certain threshold of particle size (or silver coating thickness). By exciting particles at their optimized sizes with corresponding optimized laser wavelengths, we achieved a detection limit of 100 pM and 80 pM for NCs and NBs, respectively. This outperforms their spherical counterparts which gave a detection limit of 1 nM.[24]

Experimental section

Chemicals and characterization

Gold chloride trihydrate ($HAuCl_4{\cdot}3H_2O$), sodium borohydride ($NaBH_4$,), hexadecyltrimethylammonium bromide (CTAB), silver nitrate ($AgNO_3$), L-ascorbic acid, cetyltrimethylammonium chloride (CTAC), 25 wt% in H_2O, thiram, sodium salicylate, and 5-bromosalicylicacid (5-BA) were purchased from Sigma Aldrich. All aqueous solutions were made using demineralized water, which were further purified with Mill-Q system (Millipore). All glassware used in the following procedures were cleaned in a bath of freshly prepared aqua regia and thoroughly rinsed in H_2O prior to use. UV–visible spectra were recorded using an Agilent 8453 UV–vis spectrophotometer with operating band spanning 200 nm to 1100 nm in solution. Transmission electron microscopy (TEM) images were acquired using a Philips CM20 TEM.

Synthesis of Au@Ag core–shell nanocubes

Various sizes of NCs were synthesized by a 3-step protocol according to a previously reported method with slight modifications.[28] In the first step, ~3 nm diameter Au nanoparticle seeds were synthesized. This was achieved simply by adding 0.6 mL of fresh ice-cooled $NaBH_4$ solution (10 mM) into a 10 mL aqueous solution containing $HAuCl_4$ (0.25 mM) and CTAB (100 mM), leading to a brownish solution. The seed solution was kept undisturbed for 3 hours at 27 °C. In the second step, the ~3 nm seed particles were enlarged to ~11 nm. This was achieved by adding 0.3 mL 3 nm Au seeds into a growth solution, containing 6 mL aqueous $HAuCl_4$ (0.5 mM) solution, 6 mL aqueous CTAC solution (200 mM), and 4.5 mL of aqueous AA solution (100 mM).

In the final step, Au@Ag core–shell nanocubes (NCs) with various sizes were obtained. In a typical procedure, 0.5 mL of the 11 nm seed particles and 4.5 mL of CTAC (20 mM) aqueous solution were mixed in a 20 ml vial. After the mixture was heated at 60 °C for 20 min under magnetic stirring, a specific volume aqueous $AgNO_3$ (2 mM) and aqueous solution of AA (50 mM) and CTAC (40 mM) were simultaneously injected at a rate of 0.2 mL min^{-1} using a syringe pump. The volume of AA (50 mM) added into the reaction solution was kept the same as that of $AgNO_3$. Different volumes (0.5, 2, and 5 ml) of $AgNO_3$ were used to control the size of NCs from 15 nm to 26 nm.

To control growth of larger NCs with a size of 30 to 43 nm, less seed particles were required to be added. In this study, 0.25, 0.175 and 0.1 mL 11 nm seed particles were added into CTAC (20 mM) with a total volume of 5 mL, which was followed by heating at 60 °C for 20 min under magnetic stirring. Then 5 mL of Ag NO_3 (2 mM) solution and 5 mL of an aqueous solution containing AA (50 mM) and CTAC (40 mM) were simultaneously injected at a rate of 0.2 mL min^{-1}. After 4 hours, the vials were cooled in an ice-bath for 5 min. The samples are centrifuged at 14.5k rpm to remove excess reagents, and washed with H_2O once (13k rpm, 15 min). The products were re-dispersed in deionized water for SERS studies.

Following the above protocols, we obtained NCs with 5 different sizes ranging from 15 nm to 43 nm, and their respective concentrations were 6.65, 4.43, 2.66, 1.33, 1.16, and 0.66 nM calculated from the concentration of Au seeds.

Synthesis of Au@Ag core–shell nanocuboids

The Au@Ag nanocuboids were synthesized according to the published protocol with slight modifications.[29–31] In the first step, gold nanorods were synthesized by a seed-mediated approach.[32] Firstly, the Au seed solution was made by mixing 5 mL amount of 0.5 mM $HAuCl_4$ with 5 mL of 0.2 M CTAB solution. A 0.6 mL fresh ice-cooled 0.01 M $NaBH_4$ in cold water was added into the Au(III)–CTAB solution under vigorous stirring for 30 s. Secondly, to prepare the growth solution, 9.0 g of CTAB together with 1.1 g 5-BA were dissolved in 250 mL water in a 500 mL Erlenmeyer flask, and kept in a 60 °C water bath under stirring. The solution was allowed to cool down to 30 °C, followed by addition of 12 mL 4 mM $AgNO_3$ solution. The mixture was kept undisturbed at 30 °C for 15 minutes, after which 250 mL 1 mM $HAuCl_4$ solution was added. After 15 minutes slow stirring, 1.6 mL 80 mM AA was added, and the solution was then vigorously stirred for 30 s until it became colorless. Finally, 0.8 mL of seed solution was injected into the growth solution, and left undisturbed at 30 °C for 12 h resulting the formation of gold nanorods. The as-synthesized gold nanorods were centrifuged at 7800 rpm for 40 min, followed by re-dispersion into water. With an additional centrifugation step, gold nanorods were dissolved in 50 mL 80 mM CTAC solution for 12 hours. Thus-obtained CTAC–Au nanorod solution has a concentration of 1.75 nM based on the calibration curve.

For aspect ratio ~2.2 nanorod, 0.8 g sodium salicylate was used to replace 5-BA. As for the aspect ratio ~4.1 nanorod, 24 mL 4 mM $AgNO_3$ solution was used. The other procedure is same.

In the second step, Au@Ag core–shell nanocuboids (NBs) were synthesized following the previous method.[30,31] A mixture of 1 mL of CTAC–Au nanorod solution and 9 mL 80 mM CTAC solution in a 20 mL vial was kept in 65 °C water bath under stirring for several minutes. Different volumes (0.3, 0.6, 0.9, 1.5,

and 2.0 mL) of 10 mM $AgNO_3$ were added into the mixture, followed by the addition of 80 mM AA (half volumes of $AgNO_3$). After 3 hours reaction, the products were centrifuged at 6500 rpm for 10 min, and washed with water once. The products was redispersed in deionized water for SERS studies.

SERS studies on core–shell nanoparticles

Colloidal solutions were mixed with thiram solution, and then were sucked into a capillary glass tube. Three different lasers with a wavelength of 514, 633, and 782 nm laser were used. A 10× objective was used. The Raman signals were collected by reflection modes, with laser spot size of ~2 μm. The integration time was 10 s, and slit aperture was set at 50 μm.

Results and discussion

We first used Au@Ag core–shell nanocubes (NCs) to illustrate the size dependent SERS activities. With ~11 nm gold nanoparticle as the core, a uniform silver shell could be coated with tunable thickness.[28] We deliberately synthesized NCs with six different sizes – side lengths of 14.9 ± 2.1, 20.3 ± 1.8, 25.5 ± 2.1 29.7 ± 2.0, 35.8 ± 1.9 and 42.5 ± 2.6 nm, which were named NC15, NC20, NC26, NC30, NC36 and NC43, respectively (Fig. 1a). As shown in Fig. 1b, monodisperse NCs could be obtained with a high yield.

Corresponding to silver coating thickness increase, the characteristic silver plasmonic properties began to govern the overall spectra with evident increase in resonance intensity accompanying gradual red-shift (Fig. 2a).[33,34] When the Ag shell thickness exceeds about 3 nm (Fig. 2a), LSPR of the Au core gets completely screened. Only the optical property of Ag shells is dominant. Comparing with similar size of Ag nanocubes, ~20 nm red-shift was observed here.[35] The plasmon band located at 350 nm represents the edge-associated plane multiple mode, and the dominant plasmon resonance can be attributed to the corner dipole mode respectively.[30]

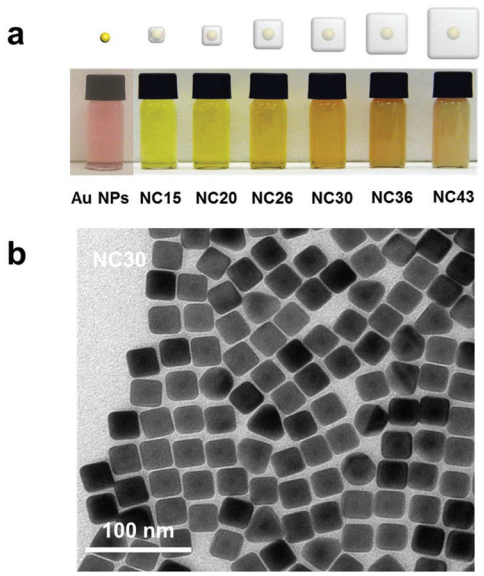

Fig. 1 Synthesis of plasmonic Au@Ag core–shell NCs with tunable sizes. (a) 6 different NC samples used in this work and their corresponding colloidal solution. (b) A typical TEM image of NC30.

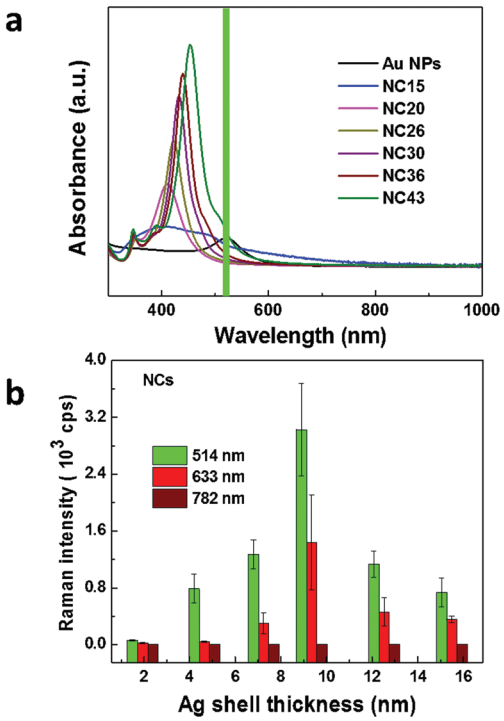

Fig. 2 The size-dependent optical properties of Au@Ag plasmonic core–shell nanocubes and SERS activities. (a) UV spectra of different sizes of Au@Ag nanocubes (green vertical line indicates the optimized laser wavelength); (b) SERS intensity of 10^{-6} M thiram at peak 1386 cm^{-1} based on increasing sizes of Au@Ag nanocubes, under three lasers of 514, 633, and 782 nm.

Under the same conditions, we systematically investigated the SERS activities of six different NCs. 100 μL thiram with specific concentrations was added into 900 μL of ~0.33 nM NCs colloidal solution, followed by shaking for 1 hour. No aggregation of nanoparticles were observed after the absorption of thiram (Fig. S4†), indicating that our method is individual particle-based SERS technique. Then, the mixture solution was introduced into a capillary glass tube mounted to a glass slide before Raman tests.

With the excitation of 514 nm laser, characteristic peaks for thiram could be clearly identified. The strongest peak is at 1386 cm^{-1}, which is the CN stretching mode and symmetric CH_3 deformation mode. 1445 cm^{-1} is attributed to the antisymmetric n (CH_3) stretch. The CN stretching vibrations and rocking CH_3 modes occur at 1146 cm^{-1} and 1517 cm^{-1}. The peak at 561 cm^{-1} is attributed to the S–S stretching mode.[36,37] (Fig. S1a†). The peak intensities at 1386 cm^{-1} for the six different core–shell NCs were compared (Fig. 2b, green histograms). Clearly, the SERS activities increased as the core–shell particle sizes increased until reaching a maximum when particle size was ~30 nm (Ag shell ~9.4 nm). After this threshold size, the SERS activity decreased.

SERS spectra were also acquired with the excitation laser of 633 nm (Fig. S1c†). Interestingly, similar trends of SERS intensity changes at 1386 cm^{-1} were observed (Fig. 2b, red histograms) and the maximum intensity was also achieved when particle size was 30 nm. This phenomenon is consistent with the previous report on the spherical core–shell nanoparticles.[24,38]

The mechanism of shell-thickness-dependent Raman enhancement with NCs can be explained by enhanced plasmonic behaviors through plasmon hybridization model, which demonstrates the interaction between the plasmons of metallic nanostructures.[39] As the coating of the Ag shell increases, the plasmon resonances shows blue shifts as depicted in Fig. 2a (Au NPs, and NC15). With further increase of Ag shell thickness, cube-cavity resonance become strongest (~9.4 nm of NCs). The intensity of antibonding plasmons will exhibit appreciable increase due to the fact that internal and external energy modes are closer.[40] Therefore, SERS intensity gets maximized due to the more intense SPR. With continuous increase of Ag shell thickness, resonance of silver shell grows as strong as that of pure silver nanocubes with the energy dissipation in the gold core.[41] The SPR of core–shell nanoparticles will decrease due to the weaker interaction of internal and external energy modes, as well as the SERS activity.

However, the SERS peak intensities also depend on the excitation laser wavelength used.[42] The relative peak intensity changes for 514 nm laser were all greater than those for 633 nm laser. When a 782 nm laser was used, the characteristic Raman peaks of thiram couldn't be identified except for the peak at ~1386 cm^{-1} (Fig. S1e†), which had a low intensity weakly dependent on nanoparticle size (Fig. 2b, histograms with red-wine color). This is due to the fact that maximum plasmonic peak is >300 nm from the excitation wavelength, hence, SERS enhancement could barely be observed.

We further investigated size- and shape-dependent Raman activity of core–shell nanoparticles using Au@Ag core–shell nanocuboides (NBs). Gold nanorods (45.6 ± 2.6 nm × 13.9 ± 1.6 nm) were prepared as the core, and silver coating thickness was systematically adjusted from ~3.0 nm to ~14.4 nm at the side, ~1.1 nm to 8.1 nm at the end (Fig. 3a), leading to the Au@Ag core–shell nanocuboids with five different sizes—47.5 ± 2.9 nm × 21.0 ± 2.1 nm, 52.5 ± 3.8 nm × 27.4 ± 3.3 nm, 55.3 ± 3.7 nm × 35.4 ± 3.1 nm, 57.2 ± 3.1 nm × 36.4 ± 2.7 nm, 61.1 ± 2.6 nm × 43.8 ± 3.2 nm, which were named as NB03, NB06, NB09, NB15 and NB20, respectively. A typical TEM image of NB15 is shown in Fig. 3b, demonstrating high monodispersity of core–shell NBs.

Different from NCs, NBs showed distinctive SPR properties with more complicated resonance modes. The core gold nanorods exhibited two characteristic peaks at 514 nm and 720 nm, corresponding to the transverse and longitudinal plasmon resonances, respectively (Fig. 4a). With coating of Ag shell, the longitudinal plasmon resonances were observed to blue shift, while the transverse plasmon resonances showed first blue shifts and then red shifts. The other two plasmon resonances showed slight red shifts with increase of Ag coating thickness, which are contributed to octapolar modes.[30,31]

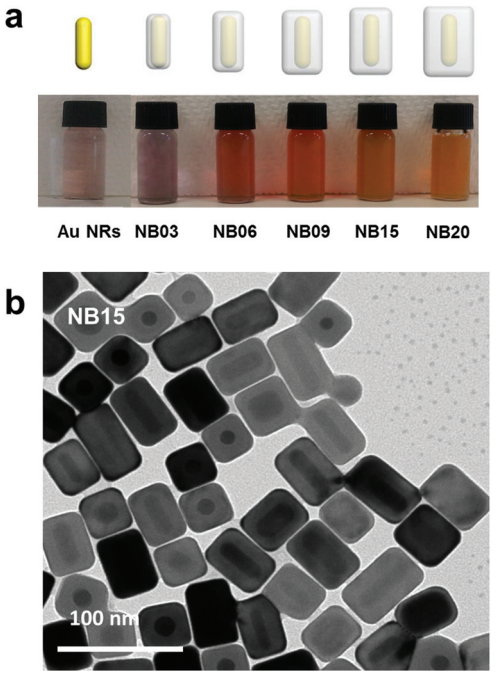

Fig. 3 Synthesis plasmonic Au@Ag core–shell nanocuboids with finely-tunable sizes. (a) 5 different NC samples used in this work and their corresponding colloidal solution. (b) A typical TEM image of NB15.

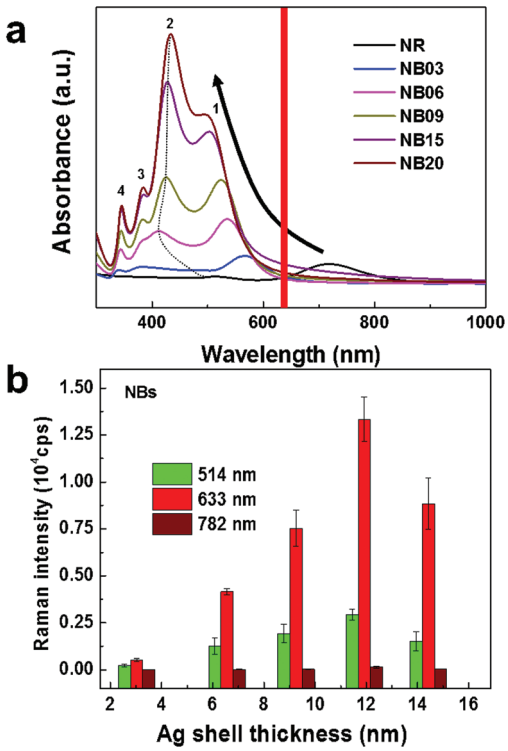

Fig. 4 The size-dependent optical properties of Au@Ag plasmonic core–shell nanocuboids and SERS activities. (a) UV spectra of different sizes of Au@Ag nanocuboids (red vertical line indicates the optimized laser wavelength); (b) SERS intensity of 10^{-6} M thiram at peak 1386 cm^{-1} based on increasing sizes of Au@Ag nanocubes, under three lasers of 514, 633, and 782 nm.

Following the same conditions for core–shell NCs, the SERS activities of NB03, NB06, NB09, NB15 and NB20 were examined when excited by three lasers (Fig. S1 b, e, f†). The characteristic Raman peaks could be identified with the core–shell NBs but the SERS enhancement exhibited an evident dependence on nanoparticle sizes (Fig. 4b). For 514 nm and 613 nm excitation lasers, the measured SERS intensity at 1386 cm^{-1} for five different NBs exhibited the similar Ag shell thickness-dependent trend. The SERS activity increased when nanoparticle sizes increased and reached a threshold size of NB15 with Ag shell thickness of ~11.9 nm × ~8.1 nm. After which the SERS activity decreased when particle size increased further. It appears that core–shell NBs discriminated the laser excitation wavelength and the maximum SERS intensities were observed at the 633 nm laser for all the five differently sized NBs considered in the study (Fig. 4b).

One can intuitively guess that the strongest activity at a SERS peak is observed when (1) the excitation wavelength closely matches that peak and (2) there is substantial absorption by plasmonic nanostructures to provide Raman enhancement.[42] Therefore, for both the cases of NCs and NBs the strongest Raman intensity would have been observed at the longest excitation wavelength being closest to the characteristic SERS peak (here, 1386 cm^{-1}), provided there is significant local electric field confinement on the plasmonic nanostructures. However, due to the narrowness of LSPR peak of NC30, significant absorption of incident excitation can only be observed at 514 nm, which provides strong localized electric field and the corresponding SERS enhancement. It can be easily seen from the UV spectra that at 633 nm and 782 nm (Fig. 2a), the absorption is negligible that leads to very weak SERS activity, and hence 514 nm is found here to be the optimum wavelength for further SERS studies.

Similar theory also explains the reason why the strongest SERS activity for NB15 is seen at 633 nm. Notice from the UV spectra (Fig. 4a) that absorbance of incident light at 782 nm is too low to be able to produce strong SERS intensity. Excitation at 514 nm would benefit from larger localized field as compared to 633 nm, however the stronger SERS activity can still be attained at 633 nm which is relatively closer to the characteristic Raman peak of thiram at 1386 cm^{-1}.

By extracting data from the recent report on core–shell nanospheres on SERS detection of thiram,[24] we formulated a figure of shape-dependent SERS activities with threshold of Ag shell thicknesses (Fig. 5a). The SERS intensity increases as the shell thickness increases until reaching a threshold value for all three shapes: spherical, cubic, and cuboid (the threshold Ag shell thickness of sphere, ~7 nm collected from ref. 20). The threshold value depends on both shapes of core and shells. Among the three shapes of core–shell particles, NBs have nonspherical core and nonspherical shell, giving the largest threshold value, ~11.9 nm at the side, which is also beyond the theoretical expectation range of 5–10 nm[41] for the spherical core–shell nanoparticles.

In addition, both NC30 and NB15 show much stronger SERS activity than spherical nanoparticles due to huge electric

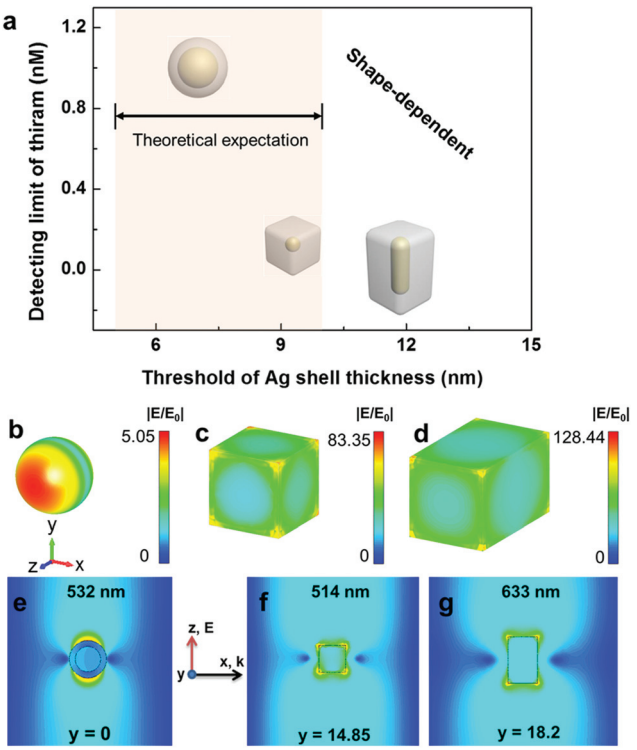

Fig. 5 (a) The shape-dependent SERS activity of Au@Ag plasmonic core–shell nanoparticles (note that, the Ag shell thickness of NBs was recorded along the length of NBs due to the strong longitudinal dipolar plasmon mode). (b)–(d) Normalized electric field ($|E/E_0|$) distribution on the surface of Au@Ag (b) nanosphere[24] (30/44 diameters in nm), (c) nanocube (NC30), and (d) nanocuboid (NB15) at incident laser wavelengths of 532, 514, and 633 nm, respectively. Note that the origin is at the centre of each nanoparticle. (e)–(f) The near-field distribution pattern of these nanoparticles calculated along a particular *y*-plane depicting the centre plane for (b) nanosphere and top surfaces of (c) nanocube and (d) nanocuboid, where the strongest electric field confinement takes place—resulting in the strongest SERS activity.

field enhancement and confinement at sharp corners. NB15 is expected to exhibit comparatively stronger localized electric field than NC30 owing to its larger cross-sectional area supporting more intense longitudinal plasmon mode. From the near-field distribution pattern, one can roughly estimate the SERS activity of a nanostructure, as SERS enhancement factor (EF) is proportional to the fourth power of *E*-field enhancement factor [*i.e.*, EF ∝ $(|E/E_0|)^4$]. As shown in Fig. 5b–g, the electric field is highly enhanced and confined around the sharp corners of the nanocube and nanocuboid, which directly attributes to enormous increase in SERS activity of these nanoparticles as compared to the spherical nanoparticle. From *E*-field enhancement factors of 5.04, 83.35, and 128.44 for Au@Ag nanosphere, nanocube, and nanocuboid (with optimized Ag shell thickness), respectively, the resulting SERS EFs can be approximated to be around 645.24, 48.26 × 10^6, and 272.15 × 10^6, respectively—indicating the strongest SERS activity in case of the nanocuboid NB15.

Furthermore, we also change the aspect ratio of nanorods nanorod core, ~2.2 and ~4.1 (Fig. S5†) to study the core-shape

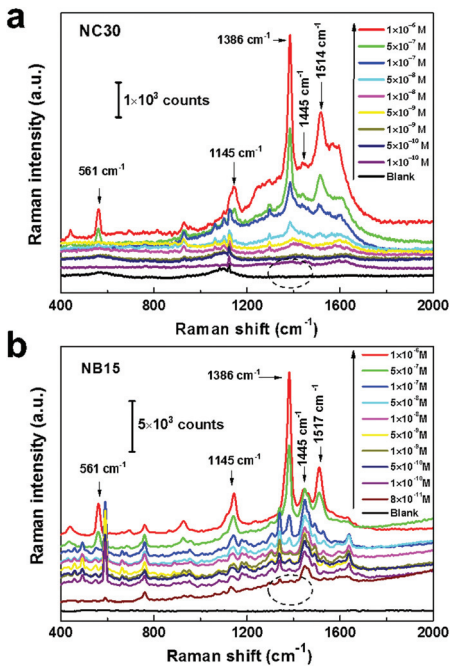

Fig. 6 The sensitivity to various concentrations of thriam based on (a) NC30 and (b) NB15.

dependent SERS activities. Longer and shorter Au nanorod core will bring down the SERS activities, as well as the sacrifice of the detecting limit of thiram (Fig. S8†).

Finally, with systematic studies of laser wavelengths and particle sizes (Fig. 2b, 4b), we conclude that NC30 and NB15 are the best SERS enhancers for their respective shapes. Therefore, we further compared their detection limits of thiram (Fig. 6). By monitoring the intensity of the strong band of 1386 cm^{-1}, as low as ~100 pM thiram (Fig. 6a) in water can be clearly detected by NC30, and 80 pM (Fig. 6b) by NB15 particle. Although there are some other attempts to detect thiram by SERS technique,[24,43–46] the lowest detecting limits has been achieved by our method. The huge Raman enhancement mainly comes from anisotropic shape with sharpness of cube or cuboid morphology[34,47] and unique core–shell structure.[24,40]

Moreover, the detecting limit in our experiment is much lower than the maximal residue limit (MRL) of 7 ppm in fruit prescribed by the U.S. Environmental Protection Agency (EPA). Our simple and rapid detection method based on NC30 and NB15 shows great potential in pesticide residue detecting and chemical sensing.

Conclusions

We have demonstrated an efficient strategy for the size/shape-dependent SERS activities of plasmonic core–shell nanoparticles towards detection of pesticide thiram. Monodisperse Au@Ag nanocubes (NCs) and Au@Ag nanocuboids (NBs) were synthesized with well controlled sizes and shapes by coating silver, and the Ag shell thickness was finely tuned from ~1 nm to ~16 nm. All these nanoparticles have been explored as SERS substrates for thiram detection, and the Raman intensities with three different lasers (514 nm, 633 nm and 782 nm) were recorded and compared. Our results clearly show that the excitation wavelength discriminated particle shapes regardless of particle sizes, and maximized Raman enhancement was observed when the excitation wavelength closely matches that SERS peak provided there is significant local electric field confinement on the plasmonic nanostructures at that wavelength; the maximum Raman enhancement was achieved at a certain threshold of particle size (or silver coating thickness). With the optimized particle size at respective optimized laser excitation wavelength, we achieved a detection limit of 100 pM and 80 pM for thiram based on NCs and NBs substrates, respectively.

Numerical modeling

The numerical simulations were performed using CST Microwave Studio™ Suite. The frequency-domain FEM solver was used to obtain the near-field distribution pattern in and around the nanoparticles at a particular wavelength of the incident light. Open boundaries were implemented to surround the target nanoparticle so that incident waves can pass those boundaries with minimal reflections, thus essentially emulating a perfectly matched layer (PML) condition. Tetrahedral mesh, which is more accurate at metallic material interfaces, was used in simulations with automatic mesh refinement to study the electric field distribution pattern. We estimated the relative permittivity of the constituent materials of the nanostructures from the bulk permittivity values of gold and silver,[48] along with size-dependent corrections[49,50] whenever the shell thickness is less than the mean free path of electron in that material. In all the simulations, the nanostructures are considered to be immersed in aqueous solution with relative permittivity of 1.7689.

Acknowledgements

This work is financially supported by ARC discovery projectes DP120100170 and DP140100052. The authors also acknowledge the use of facilities in the Melbourne Centre for Nanofabrication by the program of MCN technology fellows. P. Z. Guo acknowledges the scholarship from China Scholarship Council. The work of D. Sikdar is supported by Victoria India Doctoral Scholarship. The work of M. Premaratne is supported by ARC Discovery Grants DP110100713 and DP140100883.

Notes and references

1 M. Moskovits, *Rev. Mod. Phys.*, 1985, **57**, 783–826.
2 X. Qian, X.-H. Peng, D. O. Ansari, Q. Yin-Goen, G. Z. Chen, D. M. Shin, L. Yang, A. N. Young, M. D. Wang and S. Nie, *Nat. Biotechnol.*, 2007, **26**, 83–90.

3 S. E. J. Bell and N. M. S. Sirimuthu, *Chem. Soc. Rev.*, 2008, **37**, 1012–1024.
4 X. M. Qian and S. M. Nie, *Chem. Soc. Rev.*, 2008, **37**, 912–920.
5 W. E. Smith, *Chem. Soc. Rev.*, 2008, **37**, 955–964.
6 P. L. Stiles, J. A. Dieringer, N. C. Shah and R. P. Van Duyne, *Annu. Rev. Anal. Chem.*, 2008, **1**, 601–626.
7 K. A. Willets, *Anal. Bioanal. Chem.*, 2009, **394**, 85–94.
8 M. Vendrell, K. K. Maiti, K. Dhaliwal and Y.-T. Chang, *Trends Biotechnol.*, 2013, **31**, 249–257.
9 S. Schlücker, *Angew. Chem., Int. Ed.*, 2014, **53**, 4756–4795.
10 L. Yang, L. Ma, G. Chen, J. Liu and Z.-Q. Tian, *Chem. – Eur. J.*, 2010, **16**, 12683–12693.
11 J. Y. Xu, J. Wang, L. T. Kong, G. C. Zheng, Z. Guo and J. H. Liu, *J. Raman Spectrosc.*, 2011, **42**, 1728–1735.
12 J. C. Carter, W. E. Brewer and S. M. Angel, *Appl. Spectrosc.*, 2000, **54**, 1876–1881.
13 S. E. J. Bell and N. M. S. Sirimuthu, *Analyst*, 2004, **129**, 1032–1036.
14 G. Aragay, F. Pino and A. Merkoçi, *Chem. Rev.*, 2012, **112**, 5317–5338.
15 Z. Zhu, T. Zhu and Z. Liu, *Nanotechnology*, 2004, **15**, 357.
16 C. E. Talley, J. B. Jackson, C. Oubre, N. K. Grady, C. W. Hollars, S. M. Lane, T. R. Huser, P. Nordlander and N. J. Halas, *Nano Lett.*, 2005, **5**, 1569–1574.
17 J. B. Jackson and N. J. Halas, *Proc. Natl. Acad. Sci. U. S. A.*, 2004, **101**, 17930–17935.
18 S. J. Tan, M. J. Campolongo, D. Luo and W. Cheng, *Nat. Nanotechnol.*, 2011, **6**, 268–276.
19 M. B. Cortie and A. M. McDonagh, *Chem. Rev.*, 2011, **111**, 3713–3735.
20 K. J. Si, D. Sikdar, Y. Chen, Z. Xu, Y. Tang, W. Xiong, P. Guo, S. Zhang, Y. Lu, Q. Bao, W. Zhu, M. Premaratne and W. Cheng, *ACS Nano*, 2014, 11086–11093.
21 Z. Zhu, H. Meng, W. Liu, X. Liu, J. Gong, X. Qiu, L. Jiang, D. Wang and Z. Tang, *Angew. Chem., Int. Ed.*, 2011, **50**, 1593–1596.
22 L. He, Y. Liu, J. Liu, Y. Xiong, J. Zheng, Y. Liu and Z. Tang, *Angew. Chem., Int. Ed.*, 2013, **52**, 3741–3745.
23 W. Liu, Z. Zhu, K. Deng, Z. Li, Y. Zhou, H. Qiu, Y. Gao, S. Che and Z. Tang, *J. Am. Chem. Soc.*, 2013, **135**, 9659–9664.
24 B. Liu, G. Han, Z. Zhang, R. Liu, C. Jiang, S. Wang and M.-Y. Han, *Anal. Chem.*, 2011, **84**, 255–261.
25 A. K. Samal, L. Polavarapu, S. Rodal-Cedeira, L. M. Liz-Marzán, J. Pérez-Juste and I. Pastoriza-Santos, *Langmuir*, 2013, **29**, 15076–15082.
26 J. F. Li, Y. F. Huang, Y. Ding, Z. L. Yang, S. B. Li, X. S. Zhou, F. R. Fan, W. Zhang, Z. Y. Zhou and D. Y. Wu, *Nature*, 2010, **464**, 392–395.
27 G. Baker and D. Moore, *Anal. Bioanal. Chem.*, 2005, **382**, 1751–1770.
28 Y. Ma, W. Li, E. C. Cho, Z. Li, T. Yu, J. Zeng, Z. Xie and Y. Xia, *ACS Nano*, 2010, **4**, 6725–6734.
29 Y. Okuno, K. Nishioka, A. Kiya, N. Nakashima, A. Ishibashi and Y. Niidome, *Nanoscale*, 2010, **2**, 1489–1493.
30 R. Jiang, H. Chen, L. Shao, Q. Li and J. Wang, *Adv. Mater.*, 2012, **24**, OP200–OP207.
31 W. Xiong, D. Sikdar, M. Walsh, K. J. Si, Y. Tang, Y. Chen, R. Mazid, M. Weyland, I. D. Rukhlenko, J. Etheridge, M. Premaratne, X. Li and W. Cheng, *Chem. Commun.*, 2013, **49**, 9630–9632.
32 X. Ye, L. Jin, H. Caglayan, J. Chen, G. Xing, C. Zheng, V. Doan-Nguyen, Y. Kang, N. Engheta, C. R. Kagan and C. B. Murray, *ACS Nano*, 2012, **6**, 2804–2817.
33 J. Gong, F. Zhou, Z. Li and Z. Tang, *Langmuir*, 2012, **28**, 8959–8964.
34 L. J. Sherry, S.-H. Chang, G. C. Schatz, R. P. Van Duyne, B. J. Wiley and Y. Xia, *Nano Lett.*, 2005, **5**, 2034–2038.
35 Y. Wang, Y. Zheng, C. Z. Huang and Y. Xia, *J. Am. Chem. Soc.*, 2013, **135**, 1941–1951.
36 J. S. Kang, S. Y. Hwang, C. J. Lee and M. S. Lee, *Bull. Korean Chem. Soc.*, 2002, **23**, 1604–1610.
37 S. Sánchez-Cortés, C. Domingo, J. V. García-Ramos and J. A. Aznárez, *Langmuir*, 2001, **17**, 1157–1162.
38 B. Aswathy, G. Sony and K. G. Gopchandran, *Plasmonics*, 2014, 1–9.
39 E. Prodan, C. Radloff, N. J. Halas and P. Nordlander, *Science*, 2003, **302**, 419–422.
40 O. Peña-Rodríguez and U. Pal, *Nanoscale Res. Lett.*, 2011, **6**, 1–5.
41 O. Pena-Rodriguez and U. Pal, *Nanoscale*, 2011, **3**, 3609–3612.
42 C. L. Haynes and R. P. Van Duyne, *J. Phys. Chem. B*, 2003, **107**, 7426–7433.
43 C. Yuan, R. Liu, S. Wang, G. Han, M.-Y. Han, C. Jiang and Z. Zhang, *J. Mater. Chem.*, 2011, **21**, 16264–16270.
44 B. Saute, R. Premasiri, L. Ziegler and R. Narayanan, *Analyst*, 2012, **137**, 5082–5087.
45 B. Saute and R. Narayanan, *Analyst*, 2011, **136**, 527–532.
46 X. Zheng, Y. Chen, Y. Chen, N. Bi, H. Qi, M. Qin, D. Song, H. Zhang and Y. Tian, *J. Raman Spectrosc.*, 2012, **43**, 1374–1380.
47 C. J. Orendorff, A. Gole, T. K. Sau and C. J. Murphy, *Anal. Chem.*, 2005, **77**, 3261–3266.
48 P. B. Johnson and R. W. Christy, *Phys. Rev. B: Solid State*, 1972, **6**, 4370–4379.
49 D. Sikdar, I. D. Rukhlenko, W. Cheng and M. Premaratne, *Biomed. Opt. Express*, 2013, **4**, 15–31.
50 D. Sikdar, I. Rukhlenko, W. Cheng and M. Premaratne, *Plasmonics*, 2014, **9**, 659–672.

